

The spectral index image of the radio halo in the cluster Abell 520 hosting a famous bow shock

V. Vacca^{1,2}, L. Feretti², G. Giovannini^{1,2}, F. Govoni³, M. Murgia³, R. A. Perley⁴, and T. E. Clarke⁵

¹ Dipartimento di Fisica e Astronomia, Università di Bologna, Via Ranzani 1, I-40127 Bologna, Italy

² INAF - Istituto di Radioastronomia, Via Gobetti 101, I-40129 Bologna, Italy

³ INAF - Osservatorio Astronomico di Cagliari, Via della Scienza 5, 09047 Selargius (CA), Italy

⁴ National Radio Astronomy Observatory, Socorro, NM 87801, USA

⁵ Naval Research Laboratory Remote Sensing Division, Code 7213 4555 Overlook Ave SW, Washington, DC 20375, USA

Received MM DD, YY; accepted MM DD, YY

ABSTRACT

Context. Synchrotron radio emission is being detected from an increasing number of galaxy clusters. Spectral index images are a powerful tool to investigate the origin, nature, and connection of these sources with the dynamical state of the cluster.

Aims. The aim of this work is to investigate the spectral index distribution of the radio halo in the galaxy cluster A520, a complex system from an optical, radio, and X-ray point of view.

Methods. We present deep Very Large Array observations in total intensity at 325 and 1400 MHz. We produced and analyzed spectral index images of the radio halo in this frequency range at a resolution of 39'' and 60'' and looked for possible correlations with the thermal properties of the cluster.

Results. We find an integrated radio halo spectral index $\alpha_{325}^{1400} \sim 1.12$. No strong radial steepening is present and the spectral index distribution is intrinsically complex with fluctuations only partially due to measurement errors. The radio halo integrated spectral index and the cluster temperature follow the global trend observed in other galaxy clusters although a strong point-to-point correlation between the spectral index and the thermal gas temperature has not been observed.

Conclusions. The complex morphology in the spectral index image of the radio halo in A520 is in agreement with the primary models for radio halo formation. The flatness of the radial profile suggests that the merger is still ongoing and is uniformly and continuously (re-) accelerating the population of relativistic electrons responsible of the radio emission even at large (~ 1 Mpc) distances from the cluster center.

Key words. Galaxies: cluster: general – Galaxies: cluster: individual: A520 – Magnetic fields – Cosmology: large-scale structure of Universe

1. Introduction

The formation of massive galaxy clusters can be explained in the context of the hierarchical scenario as due to the collision and subsequent merger of small galaxy groups and subclusters. These phenomena are the most energetic in the Universe since the Big Bang. Energies as large as $\geq 10^{64}$ ergs (e.g. Sarazin 2002) are released in the form of shocks and turbulence that accelerate particles and compress magnetic field, leading to large-scale diffuse synchrotron sources associated with the intracluster medium (ICM) and known as radio halos and relics.

Radio halos and relics are faint ($\sim \mu\text{Jy}/\text{arcsec}^2$ at 1.4 GHz) sources extended on Mpc scales, located respectively at the center and in the outskirts of about 100 merging galaxy clusters (see Feretti et al. 2012 for a recent review). The study of radio halos and relics is of paramount importance to shed light on the history and physical properties of galaxy clusters, and to clarify the role of non-thermal components associated to the ICM. Their nature reveals very weak large scale magnetic fields, with central strengths $\sim \mu\text{G}$, fluctuation scales up to several hundreds of kpc (e.g. Vacca et al. 2010), and rarefied, very energetic populations of relativistic electrons spread over the cluster volume.

A key tool to investigate the shape of the relativistic electron spectrum and the link between thermal and non-thermal

properties in galaxy clusters is the spectral index¹ distribution of halos and relics. Spectral index images have been produced so far for just a few radio halos (e.g. Coma Giovannini et al. 1993, A665 and A2163 Feretti et al. 2004, A3562 Giacintucci et al. 2005, A2744 and A2219 Orrù et al. 2007, A2255 Pizzo & de Bruyn 2009, A2256 van Weeren et al. 2009, Kale & Dwarakanath 2010) revealing complex distributions with flattening in the regions directly influenced by ongoing mergers. Investigations of the integrated spectrum of radio halos have been performed as well, as in Coma (Thierbach et al. 2003), A2319 (Feretti et al. 1997), A754 and A1914 (Bacchi et al. 2003), A3562 (Giacintucci et al. 2005), A2256 (Brentjens 2008, Kale & Dwarakanath 2010), A697 (van Weeren et al. 2011, but see also Venturi et al. 2013). In some cases a steepening at increasing frequencies has been detected (e.g., Coma, A2319, A754, A3562) that could be due to the Sunyaev-Zel'dovich (SZ) effect (Ensslin et al. 2002, Pfrommer & Ensslin 2004) and/or to strong energy losses in the relativistic electron population. In the case of the diffuse emission of the Coma cluster Brunetti et al. (2013) recently showed that the SZ decrement does not significantly impact on the shape of the radio halo spectrum.

Despite the improvements in the capabilities of present radio interferometers and in the analysis procedures, a number

¹ Throughout this work we adopt the convention $S(\nu) \propto \nu^{-\alpha}$.

Table 1. Details of the VLA observations of Abell 520.

RA (J2000)	DEC (J2000)	ν (MHz)	Bandwidth (MHz)	Config.	Date	Duration (Hours)	Project
04:54:09.30	+02:55:21.00	328, 323	6.25	B	15,16-Apr-05	5.5	AC0776
04:54:09.30	+02:55:21.00	328, 323	6.25	C	02,03-May-04	6	AC0706
04:54:09.30	+02:55:21.00	1365, 1435	50.0	C	30-Aug-05	5	AC0776
04:54:09.30	+02:55:21.00	1365, 1435	50.0	D	13-Aug-04	7	AC0706

Col. 1, Col. 2: Observation pointing; Col. 3: Observing frequency;

Col. 4: Bandwidth; Col. 5: VLA configuration; Col. 6: Observing dates; Col. 7: Total integration time; Col. 8: Observation project.

Table 2. Information on total intensity images.

Array	ν MHz	Beam (") ²	$\sigma(I)$ mJy/beam
B	325	18 × 18	0.6
C	325	60 × 60	0.8
B+C	325	26 × 26	0.7
C	1400	16 × 16	0.025
D	1400	50 × 50	0.05
C+D	1400	26 × 26	0.03

Col. 1: VLA configuration;

Col. 2: Observing frequency;

Col. 3: Resolution of the observation;

Col. 4: rms noise of the total intensity image.

of questions concerning radio halo origin and evolution are still open. A mechanism of (re-) acceleration of relativistic electrons (primary models, e.g. Brunetti et al. 2009) or *in situ* generation (secondary models, e.g. Ensslin et al. 2011) is required to explain their emission over Mpc scales. Observational properties of radio halos, e.g. the complex radio-halo morphology and spectral index distribution, high frequency cut-off in the radio halo spectrum, and spectral radial steepening support primary model predictions. Nevertheless, Ensslin et al. (2011) show that the radio halo formation could be explained also by means of a high central energy density concentration of cosmic rays that should be typical of cluster undergoing major mergers and strongly turbulent. We have to note that at the moment neither the primary nor the secondary models allow an exhaustive description of the observational properties of radio halos. It seems more likely that relativistic electrons continuously generated by hadronic collisions and present in all galaxy clusters coexist with a population of relativistic electrons (re-) accelerated through magneto-hydro-dynamical turbulence due to cluster mergers (see Cassano 2009, and references therein). The global picture has become even more complex because of the recent discovery of radio halos in low X-ray luminosity clusters (see Giovannini et al. 2011 and references therein) that opens new questions concerning the radio halo formation processes. Detailed analysis of the radio halo emission at different frequencies are essential to shed light on these aspects.

In this paper we present the study of the spectral index of the radio halo in the galaxy cluster Abell 520 between 325 and 1400 MHz. In § 2 a description of the present radio, X-ray, and optical knowledge on A520 is given. In § 3 the radio observations and data reduction procedures are presented. In § 4 the results about the spectral index of the radio halo and the radio galaxies in A520 are shown. In § 6 we discuss the results, while in § 7 we draw our conclusions.

Throughout this paper we adopted a Λ CDM cosmology with $H_0 = 71 \text{ km s}^{-1} \text{ Mpc}^{-1}$, $\Omega_m = 0.27$, and $\Omega_\Lambda = 0.73$. At the distance of A520 ($z=0.199$, Struble & Rood 1999), $1''$ corresponds to 3.25 kpc.

2. The cluster of galaxies Abell 520

Abell 520 is a complex and interesting galaxy cluster that has been observed in the X-ray, optical, and radio domain. By analysing NRAO Very Large Array (VLA) Sky Survey (NVSS, Condon et al. 1998) images, Giovannini et al. (1999) found for the first time hints of diffuse large scale emission in this cluster, later confirmed by the work of Govoni et al. (2001). Govoni et al. (2001) reveal a wide radio halo with a largest linear size of 1.4 Mpc, elongated in the NE-SW direction, as the central X-ray emission. Indeed, the ROSAT low resolution X-ray observations indicate that the X-ray emission consists of an inner elongation in the NE-SW direction and of an outer emission in the SE-NW direction. High resolution *Chandra* X-ray observations by Govoni et al. (2004) indicate that this system is undergoing a strong merger event in the NE-SW direction. They detect a dense, cool gas clump in the South-West of the cluster, probably coming from North-East, and followed by a cool tail characterized by a strip of hot gas where the radio halo emission seems to originate from (see the bottom panel of Fig. 1).

Merger shocks have been firmly detected only in a few clusters from jumps in X-ray surface brightness and in temperature. Some examples are in A3667 (Vikhlinin et al. 2001, Sarazin et al. 2013) and in Coma (Neumann et al. 2001, Akamatsu et al. 2013, Ogrea & Brueggen 2013). Another example is given by A2146, where Russel et al. (2010) found a bow shock from a sharp discontinuity in the temperature and gas density. Deep *Chandra* observations by Markevitch et al. (2005) of A520 indicated the presence of a bow shock, previously suggested by Govoni et al. (2004), in front of the dense clump, coincident with the SW edge of the radio halo. This shock is characterized by a Mach number $M = 2.1^{+0.4}_{-0.3}$ and is the second unambiguously recognized supersonic merger shock front in a cluster that shows a sharp gas density edge and a clear temperature jump (the first one is the Bullet cluster, Markevitch et al. 2002). Markevitch et al. (2005) state that the electrons responsible for the edge of the radio halo emission in A520 may be accelerated by this shock and, in this hypothesis, they expect a slope of the radio halo spectrum $\alpha \approx 1.2$ in correspondence of the

edge. The spectrum should quickly steepen as a function of the distance from the edge in the post-shocked region, since no turbulence or other kind of acceleration mechanism are supposed to be present in between the shock and the cool tail in the NE. This trend has been observed in elongated relics, as for example in A1240 (Bonafede et al. 2009b) and in CIZA J2242.8+5301 (van Weeren et al. 2010), where the spectral index steepens toward the cluster center. On the contrary if the efficiency of the shock is not enough to accelerate the electrons, the radio edge may be caused by the compression of the magnetic field. In this scenario, they expect to detect a 10-20 times fainter radio emission with the same spectrum in front of the shock where the pre-compressed relativistic particles and magnetic fields exist.

Optical investigations by Proust et al. (2000) indicate as well a complex system hosting a concentration of galaxies at the center of the cluster with two extensions. They suggest that this cluster is a dynamically young system and these extensions are related to clumps of galaxies colliding on a dark matter gravitational well, located at the center of the X-ray emission region. This insight has been confirmed by the analysis of Jee et al. (2012). By means of a high resolution weak lensing studies carried out with Hubble Space Telescope data, they map a filamentary structure of 1.5 Mpc in size elongated in the NE-SW direction and confirm the presence of a dark matter core with a significance larger than 10σ , whose presence has been already observed by Mahdavi et al. (2007) at 4σ level. In contrast with observations in other merging galaxy clusters (e.g., the Bullet cluster, Clowe et al. 2006) and with the collisionless dark matter scenario, the dark matter core is at the same location as the X-ray luminosity distribution peak but not as the bright cluster galaxies. Results from Girardi et al. (2008) from TNG and INT observations combined with data from literature and from the CNOC team (Carlberg et al. 1996, Yee et al. 1996) suggest that the cluster formation is actually taking place at the crossing of three filaments: one in the NE-SW direction, one in the EW direction, and one almost aligned with the line of sight. The peak in the dark matter distribution could be therefore the consequence of projection effects.

By analyzing new Hubble Space Telescope data, Clowe et al. (2012) do not detect the dark matter core and, after subtraction of the X-ray plasma mass, they find a good agreement between the mass distribution in this cluster and the luminosity distribution of the cluster galaxies, and between weak lensing mass measurements and the morphology of the core galaxy-filled structure. Moreover, they find that the mass within a sphere encompassing a mean overdensity of 200 is $M_{200} = (9.1 \pm 1.9) \times 10^{14} M_{\odot}$, in agreement with previous works.

3. Radio observations and data reduction

We present archival observations (Projects AC0776 and AC0706) of A520 at 325 and 1400 MHz obtained using the Very Large Array (VLA) respectively in spectral line and in continuum mode. The observations at 325 MHz have been obtained in B and C configurations, while those at 1400 MHz are in C and D configurations. The details of the observations are summarized in Table 1. The data reduction has been performed following standard procedures using the NRAO's Astronomical Image Processing System (AIPS) package. Total intensity images were produced with the multi-scale clean technique (see e.g. Greisen et al. 2009), an extension of the classical clean algorithm imple-

mented in the task IMAGR. The fluxes are expressed according to Perley - Taylor 1999.2 scale ².

At 1400 MHz the radio source 0542+498=3C147 was used as primary flux density calibrator while the nearby source 0503+020 has been used as complex gain calibrator. Radio interferences were carefully excised. The two IFs were averaged to obtain the surface brightness image and several cycles of self-calibration and CLEAN were applied.

The 325 MHz data were obtained with a total bandwidth of 6.25 MHz, subdivided in 16 channels with a resolution of 390 kHz each. We excluded the edge channels and averaged over channels, resulting in 5 channels with a resolution of ~ 1 MHz each. The radio source 0542+498=3C147 was used as primary flux density and bandpass calibrator while the nearby source 0521+166=3C138 has been used as complex gain calibrator. Radio interferences were carefully excised with a flag of about 30% of the data. To obtain the surface brightness image we averaged the five channels of both IFs together in the gridding process using IMAGR. Since VLA images over a wide-field-of-view suffer from distortions due to the non-coplanarity of the array (Perley 1999), we cover the central $\sim 4^{\circ}$ with several small overlapping facets. Strong sources outside this area can affect the final image because their secondary lobes can be present in our field of view at this frequency. To include in the cleaning process these sources, we looked for sources with a flux larger than 0.5 Jy at 1400 MHz in a region of about $\sim 6^{\circ}$ in radius, by using the NVSS catalog. These sources have been included in the cycles of self-calibration and CLEAN applied to remove residual phase variations. After self-calibration, to better image the diffuse emission at the center of the cluster, discrete sources at a linear distance larger than ~ 1.5 Mpc have been subtracted.

Moreover, for each frequency, data corresponding to different configurations of the VLA have been combined aiming at producing images with better uv-coverage and sensitivity but still good angular resolution. The sensitivities of the final images are summarized in Table 2. We note that our sensitivity at 325 MHz in C configuration ~ 0.8 mJy/beam is slightly higher than the theoretical noise for the bandwidth and the duration of the observations (~ 0.5 mJy/beam, of the same order of the confusion limit at this frequency ~ 0.44 mJy/beam), while at 1400 MHz our sensitivity in D configuration $\sim 50 \mu\text{Jy/beam}$ is limited by the confusion.

The 1400 MHz total intensity images of the radio emission in A520 at different resolutions are shown in Fig. 1. The top left panel shows the image in D configuration where the full extent of the radio halo is visible. After correcting for the primary beam and masking the radio galaxies, from this image we measure a flux of the radio halo at 1400 MHz $S_{1400\text{MHz}} = (16.7 \pm 0.6)$ mJy. Here and in the following, the total error is the quadratic sum of the statistical error and of the systematic error. The statistical error includes calibration, while the systematic error is related with flux-scale uncertainty that has been assumed to be 3% of the measured flux in order to take into account also the bootstrap uncertainty. We note that this value of the flux differs from the 34 mJy measured by Govoni et al. (2001) probably because of differences in the subtraction of the point sources. From now on the value of (16.7 ± 0.6) mJy should be considered as the reference. Subtracting the flux of discrete sources measured with C configuration data from the total flux over the region covered by the diffuse emission measured with D configuration gives an estimation consistent with this value within the errors. A higher

² See the *VLA Calibrator Manual* <http://www.vla.nrao.edu/astro/calib/manual/baars.html>.

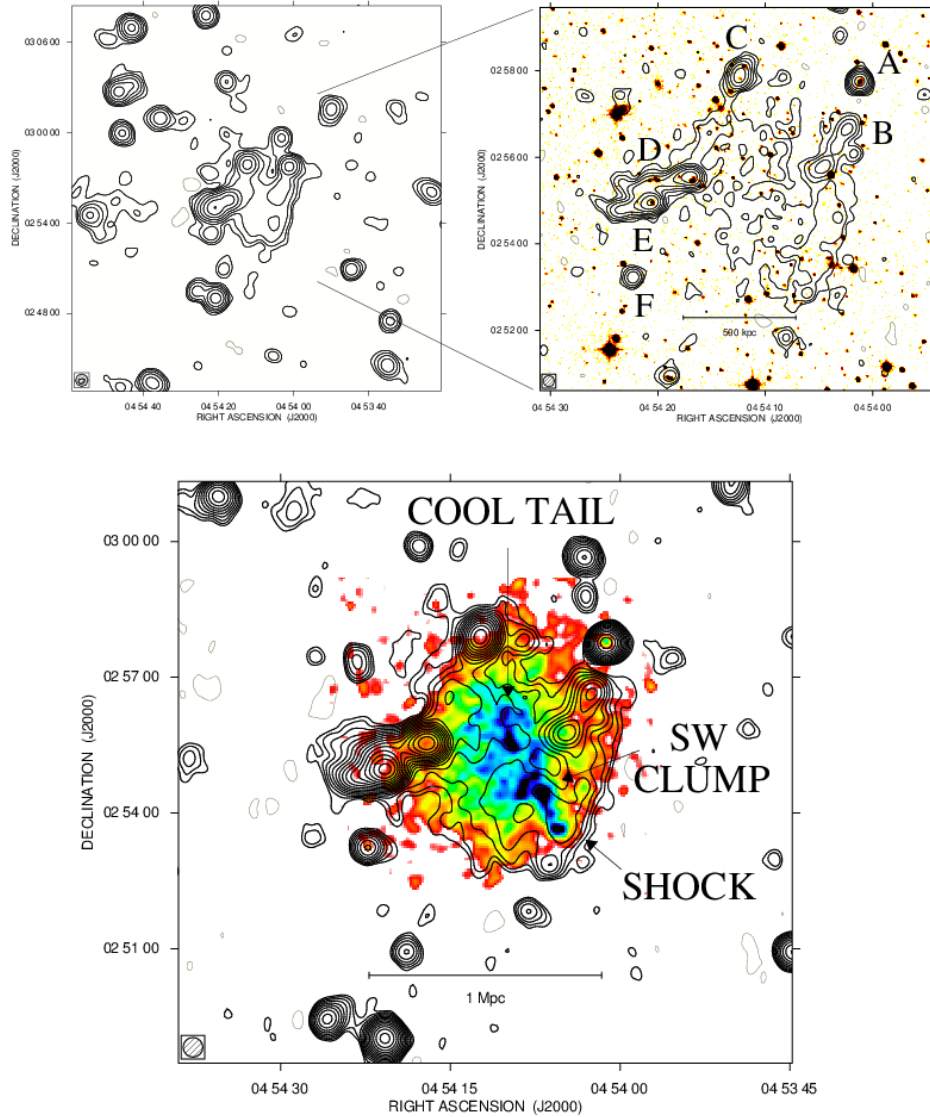


Fig. 1. *Top left panel:* total intensity radio contours at 1400 MHz (VLA in D configuration) with an FWHM of $50'' \times 50''$. The contour levels are -0.15 mJy/beam, 0.15 mJy/beam, and the rest spaced by a factor 2. *Top right panel:* total intensity radio contours at 1400 MHz (VLA data in C configuration) with an FWHM of $16'' \times 16''$. The contour levels are -75 μ Jy/beam, 75 μ Jy/beam, and the rest spaced by a factor 2. The contours of the radio intensity are overlaid on the red plate of the Sloan Digital Sky Survey. *Bottom panel:* total intensity radio contours at 1400 MHz (combining VLA data in C and D configuration) with an FWHM of $26'' \times 26''$. The contour levels are -90 μ Jy/beam, 90 μ Jy/beam, and the rest spaced by a factor $\sqrt{2}$. The contours of the radio intensity are overlaid on the ACIS-I *Chandra* X-ray adaptively smooth brightness image in the 0.8–4 keV band (Govoni et al. 2004) in colors.

resolution image obtained from the data in C configuration is shown in the top right panel, but see also Fig. 2 for a greyscale visualization. The radio contours are superposed to an optical image from the *Sloan Digital Sky Survey* red plate. Radio galaxies at the boundary of the diffuse emission can be easily identified. Some of them present an optical counterpart, i.e. the source A and the two narrow angle tailed sources D and E. In the bottom panel a combination of the datasets in D and in C configuration is shown. The radio isocontours are overlaid on an ACIS-I *Chandra* X-ray image in the 0.8–4 keV band (Govoni et al. 2004). The cluster appears characterized by substructures on scales $\gtrsim 80$ kpc both at the radio and at the X-ray wavelengths. In the cluster center as well as in the outskirts, where the bow shock has been detected, peaks and substructures in the X-ray and in the radio image have the same spatial location, indicating

a deep link between thermal and non-thermal properties in this system.

The total intensity images of the galaxy cluster at 325 MHz are shown in Fig. 3. On the top left panel, the low resolution image is presented. The radio halo appears extended as in the low resolution image at 1400 MHz (top left panel in Fig. 1), while the emission of some discrete sources observed at 1400 MHz is below the noise level in this image, giving an upper limit for their spectral index (see § 4.2). After correcting for the primary beam and masking radio galaxies, from this image we measure a flux density for the radio halo of $S_{325\text{MHz}} = (85 \pm 5)$ mJy. On the top right panel, a high resolution image at 325 MHz is shown where the radio halo emission is completely resolved. The combination of the B and C configuration observations is shown in the bottom panel.

The integrated spectral index evaluated from the above fluxes is $\alpha_{325}^{1400} = 1.12 \pm 0.05$. The spectral index of discrete radio sources are presented in § 4.2.

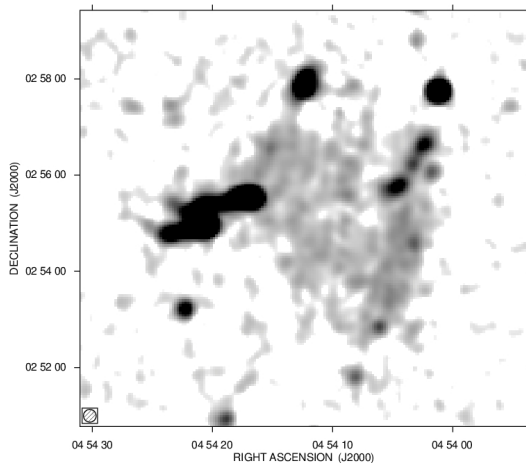


Fig. 2. Total intensity radio brightness at 1400 MHz (VLA data in C configuration) with an FWHM of $16'' \times 16''$.

4. Spectral index images

To produce spectral index images of the radio emission at the center of the cluster we compared total intensity images at 325 and 1400 MHz using images produced with the same uv-coverage, resolution and pixel size, and the Dan Briggs AIPS robustness parameter set to zero. As discussed in Orrù et al. (2007), considering only those pixels with a signal larger than 3σ at both frequencies implies a bias in the measurement of the spectral index, since regions with a flat spectrum can not be investigated. The faintest regions of the radio halo at 1400 MHz are above the noise at 325 MHz only if the radio halo spectral index is steeper than ~ 2 . To minimize this effect, in the analysis of the radial profile of the spectral index we directly compared the total intensity images at 325 and 1400 MHz without applying any cut in brightness, unless otherwise specified.

4.1. Radio halo

In Fig. 4 the image of the spectral index of the radio halo and the radio galaxies embedded in the diffuse emission and the image of the 1σ uncertainty evaluated pixel by pixel are shown at $60''$ (~ 200 kpc), top panels, and at $39''$ (~ 120 kpc), bottom panels.

The low resolution image allows better recovery of the faint structures in the North and in the South-East, where flatter spectral index values can be observed. We evaluated the spectral index in the regions indicated in Fig. 4 (top left panel) by using boxes 1.5 times the beam in size. The North (REGION1 in Fig. 4) shows an average spectral index of $\langle \alpha \rangle = 1.03$, the South-West (REGION2) of $\langle \alpha \rangle = 1.22$ and the South-East (REGION3) of $\langle \alpha \rangle = 1.23$. These values are consistent with those evaluated directly from the integrated fluxes at the two frequencies.

In Fig. 5 the azimuthally averaged brightness profile at 325 and 1400 MHz (top panel) and the consequent spectral index (bottom panel) are shown. Since we are interested on the average radial behavior of the spectral index, we measured the surface brightness from the $60''$ resolution images. Each data point with

Table 3. Statistics of the spectral index and the spectral index error images.

Beam ($''$) ²	$\langle \alpha \rangle$	$\langle Err_\alpha \rangle$
39×39	1.25	0.16
60×60	1.21	0.12

its $1-\sigma$ uncertainty represents the average brightness in concentric annuli of half-beam-width centered on the X-ray peak³, as shown in the inset. The arrows represent the upper limits at $3-\sigma$. Discrete sources have been masked out and excluded from the statistics. Their flux and spectral index are given in § 4.2. The spectral index profile of the radio halo appears rather flat.

In Fig. 6 the radio brightness at 325 and 1400 MHz (top panel) and the consequent spectral index (bottom panel) along a sector of the diffuse emission are shown. Each data point with its $1-\sigma$ uncertainty represents the average brightness in a sector of concentric annuli of beam-width centered on the shock peak and crossing the direction of propagation of the shock and the NE periphery along the cool tail, see the inset panel. To be more sensitive to small scale variations we used the total intensity images at $39''$. The brightness of the radio halo keeps flat both at 325 and at 1400 MHz, with a consequent flat spectral index.

4.1.1. Fluctuations in the radio halo spectral index image

In Table 3 the statistics of the spectral index and the spectral index error images of the radio halo both at $39''$ and at $60''$ (Fig. 4) are summarized. The mean values of the spectral index and of its error are in good agreement at the two resolutions.

The spectral index image of the radio halo appears clumpy, with fluctuations both at high and at low resolution. To investigate the nature of these fluctuations we studied the distribution of the spectral index values. We extracted the information pixel by pixel from the spectral index and the spectral index error image after masking the radio galaxies (Fig. 7) and we calculated the mean and the sigma over these values. The blue histogram refers to the $39''$ image, while the black one to the $60''$ image. The two distributions have a mean value $\langle \alpha_{60''} \rangle = 1.21$ and dispersion $\sigma_{\alpha_{60''}} = 0.23$ at $60''$, and $\langle \alpha_{39''} \rangle = 1.25$ and $\sigma_{\alpha_{39''}} = 0.22$ at $39''$. The distributions are asymmetric respect to the mean value both at high and at low resolution. Indeed, they miss the flatter spectral index values, because of the cut in total intensity applied to produce the two spectral index images.

The error image of the spectral index has been produced evaluating the uncertainty on a pixel basis, therefore if the patchy structure of the spectral index image is due to measurement errors we expect that the mean value of the error image and the dispersion of the spectral index distribution to be comparable. When compared with the mean value of the spectral index error image, the dispersion of the distributions in Fig. 7 is slightly larger both at high and at low resolution.

We conclude that the measurement errors significantly contribute to the observed fluctuations in the spectral index distribution. Moreover, the spatial frequency coverage could cause instrumental noise responsible of fluctuations on spatial scales that are about the resolution size. Nevertheless, a certain degree of intrinsic complexity seems to be present.

³ As X-ray peak we adopted the value give by Govoni et al. (2001), RA (J2000) = 04^h54^m10.6^s and DEC (J2000) = +02°55'20''.

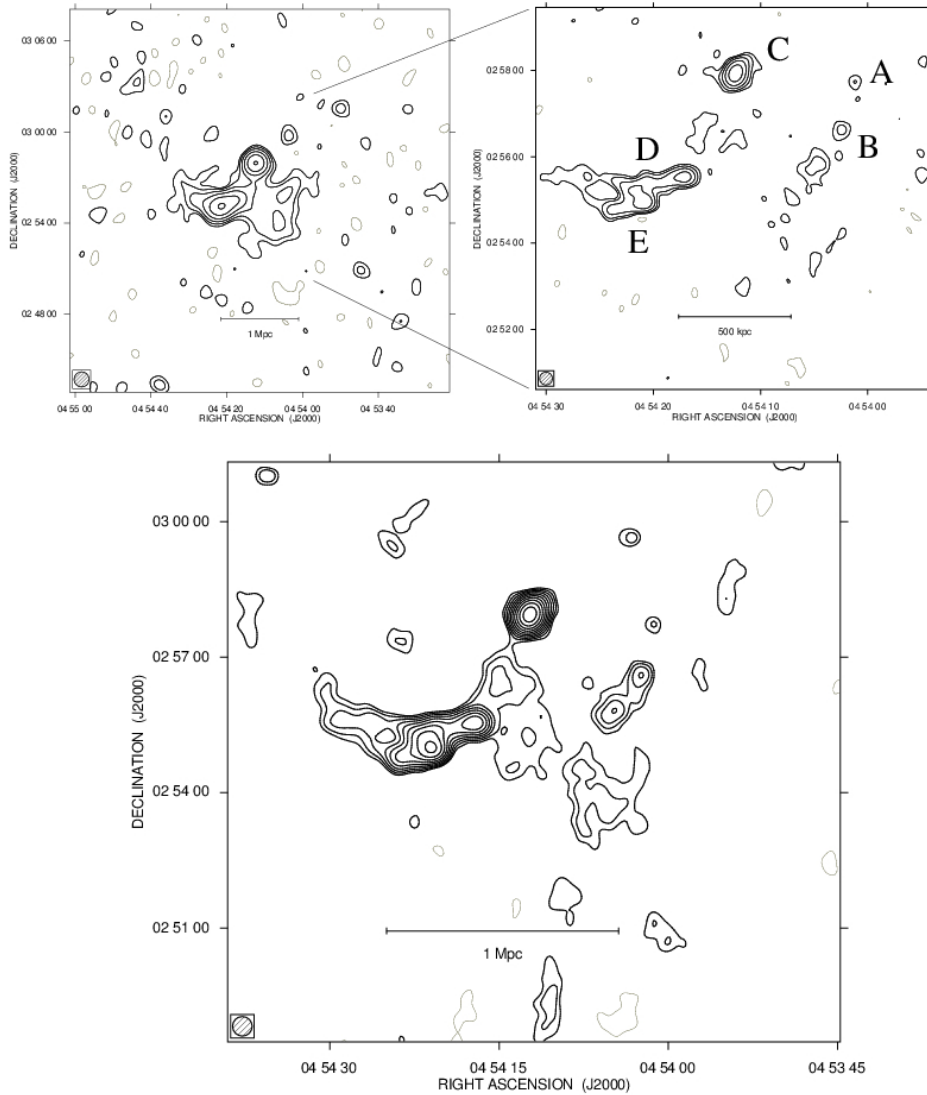


Fig. 3. *Top left panel:* total intensity radio contours at 325 MHz (VLA in C configuration) with an FWHM of $60'' \times 60''$. The contour levels are -2.4 mJy/beam, 2.4 mJy/beam and the rest spaced by a factor 2. *Top right panel:* total intensity radio contours at 325 MHz (VLA data in B configuration) with an FWHM of $18'' \times 18''$. The contour levels are -1.8 mJy/beam, 1.8 mJy/beam and the rest spaced by a factor 2. *Bottom panel:* total intensity radio contours at 325 MHz (combining VLA data in B and C configuration) with an FWHM of $26'' \times 26''$. The contour levels are -2.1 mJy/beam, 2.1 mJy/beam and the rest spaced by a factor $\sqrt{2}$.

4.1.2. Radio halo spectral index and X-ray properties of the cluster

A520 is one of the first clusters where a comparison between the shape of the radio and X-ray brightness profile has been performed (Govoni et al. 2001). They found that the two azimuthally averaged profiles do not show a close similarity as has been observed in other clusters (e.g. Coma, A2255, A2319), the radio halo being elongated while the X-ray emission quite extended and symmetric.

To infer some information about a possible link between the radio halo emission and the thermal properties of the hosting cluster we compared the spectral index with the X-ray brightness and the thermal gas temperature images. In Fig. 8 the radio halo spectral index image at $39''$ superimposed with the contours from the *Chandra* X-ray brightness image in the 0.8–4 keV band is shown. The bright region coincident with the shock detected in the X-ray image is characterized by an average spectral index

~ 1.25 that flattens to values $\sim 1-1.1$ behind (in the North-East) and in front (in the South) of the shock.

A point-to-point correlation between the radio-halo spectral index and the thermal-gas temperature has been observed for the first time in the cluster in A2744 (Orrù et al. 2007), indicating that regions of the radio halo with a flat spectrum appear characterized by higher temperatures. We looked for the existence of such a correlation for the radio halo in A520. To be more sensitive to point-to-point fluctuations in the spectral index, we used the image at $39''$. For the temperature we used the image from Govoni et al (2004). In Fig. 9 the exponential smoothing of the spectral index between 325 and 1400 MHz versus thermal gas temperature is shown. The data have been extracted pixel by pixel and then exponentially smoothed, i.e. a weighted moving average with exponential weights has been performed, with a smoothing scale of 1 keV. Discrete sources have been masked out and excluded from the statistics. The shaded region describes

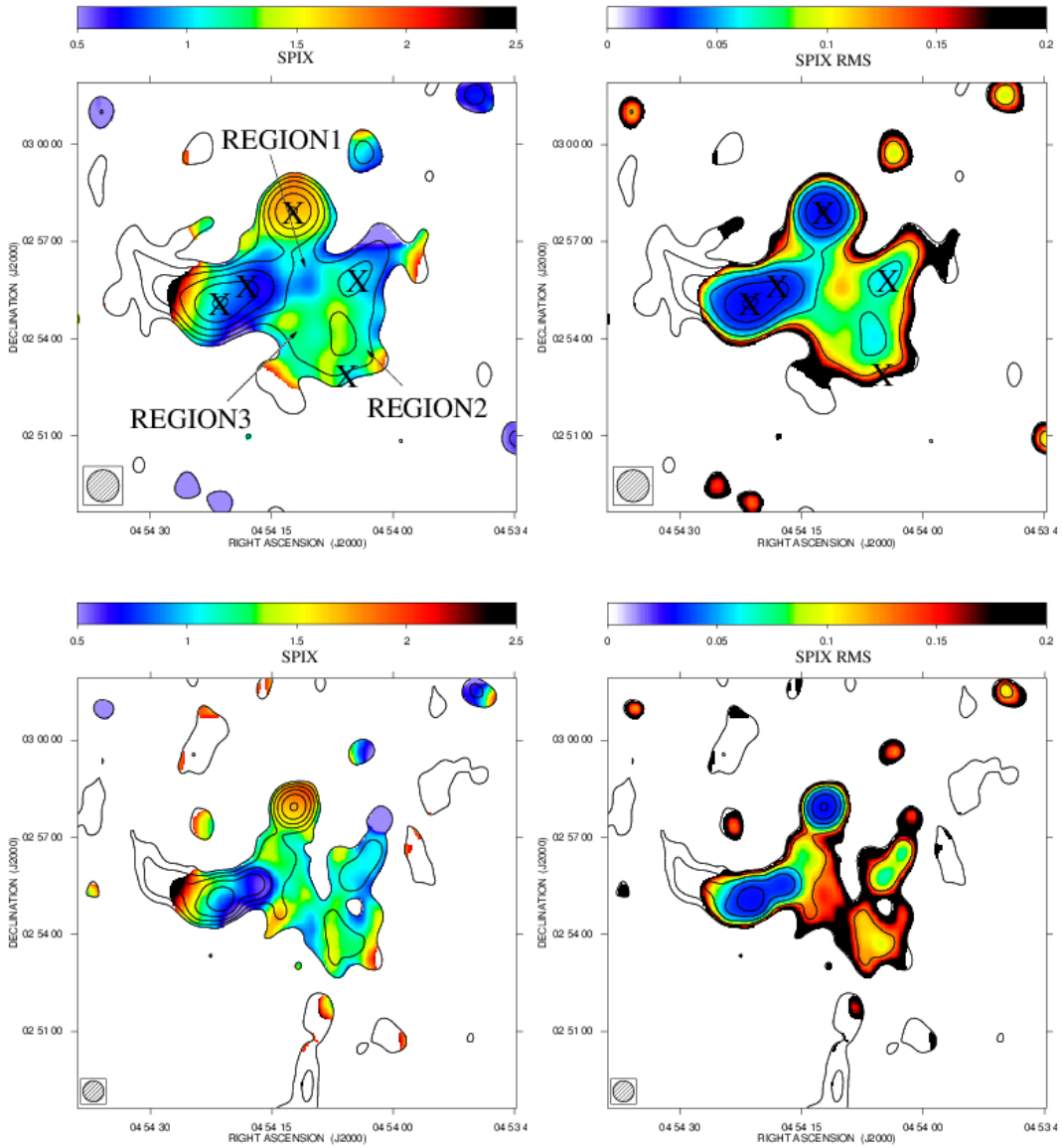


Fig. 4. Radio contours at 325 MHz overlaid on the spectral index image (left panels) and on spectral index error image (right panels) of A520 between 325 and 1400 MHz with a resolution of $60'' \times 60''$ (top panels) and $39'' \times 39''$ (bottom panels). We blanked pixels with brightness below 3σ at 325 or 1400 MHz. The crosses in the low resolution image represent the radio galaxies embedded in the diffuse emission.

the 1σ uncertainty. In the coldest regions (~ 2 keV), the spectral index is between 1.1 and 1.4. Moving to higher temperatures, e.g. in the South and in the North-East of the cluster, the spectral index decreases to ~ 0.9 with a scatter of ~ 0.05 .

If a global temperature of the thermal gas in A520 $T = (7.1 \pm 0.7)$ keV is considered according to Govoni et al. (2004), the values of spectral index and temperature observed in A520 appear to follow the trend found for the other radio halos by Giovannini et al. (2009) and Feretti et al. (2012).

4.2. Radio galaxies

A dominant radio galaxy can not be identified at the center of the cluster but several powerful sources are present in the outskirts of the diffuse radio halo emission. These radio sources are labeled in Fig. 1 and in Fig. 3 (top right panels) and their flux at 325 and 1400 MHz along with their integrated spectral indexes

are given in Table 4. Just three of them have been found to have an optical counterpart, i.e. A, D and E that have been identified as cluster members (see Cooray et al. 1998 and Girardi et al. 2008).

The sources D and E are narrow angle tail radio galaxies with size ~ 300 and 500 kpc, located in the East of the cluster and oriented in the opposite direction respect to the cluster center. Their spectra are quite similar: flatter near to the nucleus ($\alpha \sim 0.7$) and steeper moving toward the external part of the tail, up to values 1.5 and higher.

Source A is a point-like source. According to the flux measured at 1400 MHz and the upper limit inferred from the 325 MHz image, we can conclude that it is characterized by an inverted spectrum.

Sources B and F do not show an optical counterpart. The radio source F is in the South-East of the cluster and its signal is under the noise level at 325 MHz, allowing only an upper limit

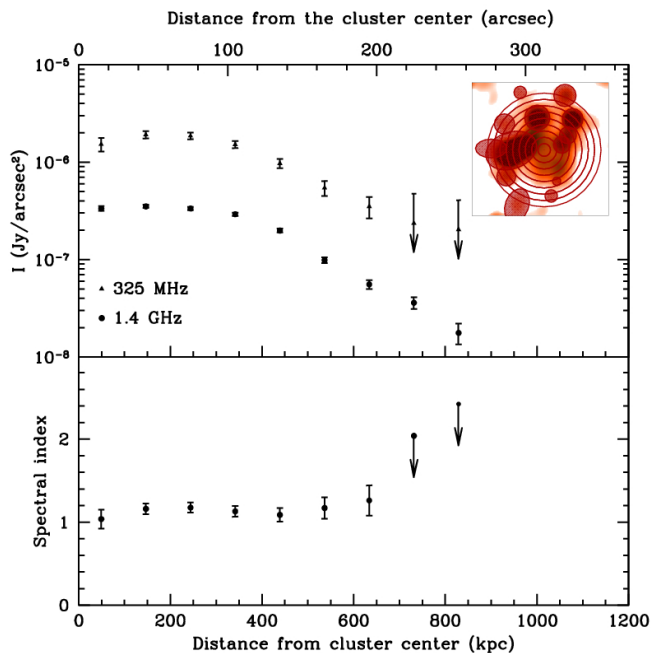


Fig. 5. *Top:* azimuthally averaged brightness of the radio halo at 325 (triangles) and 1400 MHz (circles) versus the distance from the cluster center at a resolution of $60''$. Arrows represent $3\text{-}\sigma$ upper limits. In the inset the annuli used to calculate the azimuthally averaged brightness are shown. Masks have been used to exclude discrete sources from the statistics. *Bottom:* spectral index radial profile.

on its spectral index. Source B has a double lobed structure, with size ~ 300 kpc assuming the redshift of A520, located in the West of the cluster and has a spectral index ranging across the source between 0.7 and 1.4.

Source C is a powerful source in the North, only marginally resolved at a resolution of $\sim 15''$. From Fig. 1 top right panel, two optical candidates slightly displaced from the peak of the radio source emission can be identified. This source is characterized by the steepest spectrum in the field. Between 325 and 1400 MHz its spectral index is $\alpha = 1.59 \pm 0.03$. We investigated its emission also at lower frequencies by using *VLA Low-Frequency Sky Survey Redux* (VLSSr, Lane et al. 2012). From the VLSSr image at 74 MHz we measure a flux $S_{74\text{MHz}} = (870 \pm 190)$ mJy. This flux is expressed according to the Scaife & Heald (2012) scale and has been corrected for the clean bias. In Fig. 10 the spectrum of the source between 74 and 1400 MHz is shown. From the fit of the spectrum in this range of frequencies we infer an overall averaged spectral index $\alpha = 1.60 \pm 0.03$ in good agreement with the estimate obtained by using only higher frequency data. New JVLA observations at higher resolution (Vacca et al. in preparation) reveal that the source is actually a double-lobed radio source, while its emission is under the noise level at 5000 MHz. The steep spectrum, the possible displacement between the radio and optical emission and the double lobed structure of this source suggest that it could be classified as a dying source (e.g. Parma et al. 2007, Murgia et al. 2011). Alternatively, this source could be the radio counterpart of an high-redshift typical cluster-member elliptical-galaxy not detected in optical surveys because of sensitivity reasons.

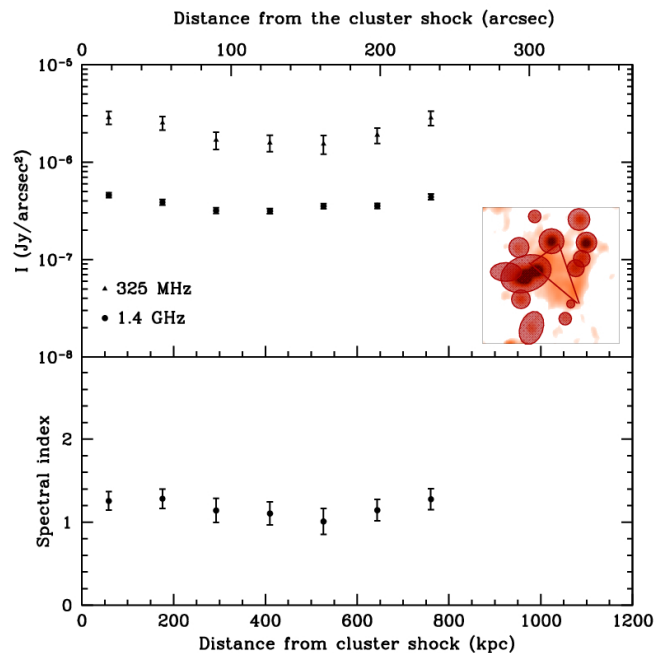


Fig. 6. *Top:* azimuthally averaged brightness of the radio halo at 325 (triangles) and 1400 MHz (circles) in a sector of concentric annuli versus the distance from the shock peak at a resolution of $39''$. The sector starts from the South-West and crosses the cluster towards the North-East, see the inset. *Bottom:* spectral index along the sector.

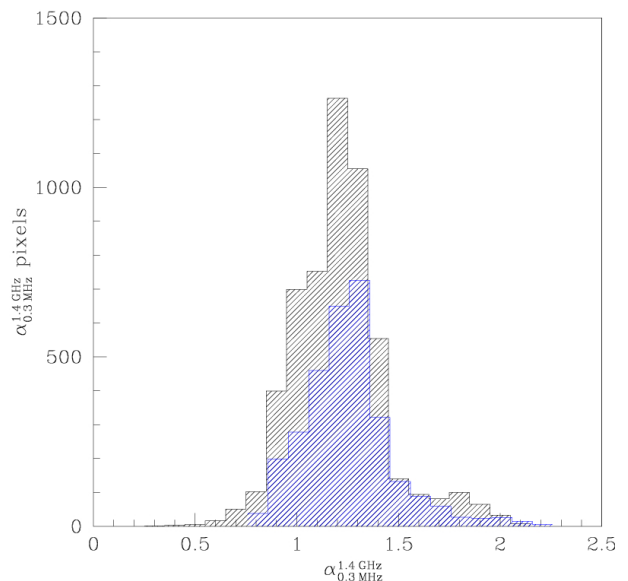


Fig. 7. Histogram of the spectral index values from the image at $60''$ (black) and $39''$ (blue) resolution. These distributions have a mean value and a dispersion $\langle \alpha_{60''} \rangle = 1.21$ and $\sigma_{\alpha_{60''}} = 0.23$ at $60''$ and $\langle \alpha_{39''} \rangle = 1.25$ and $\sigma_{\alpha_{39''}} = 0.22$ at $39''$.

5. Radio halo brightness profile

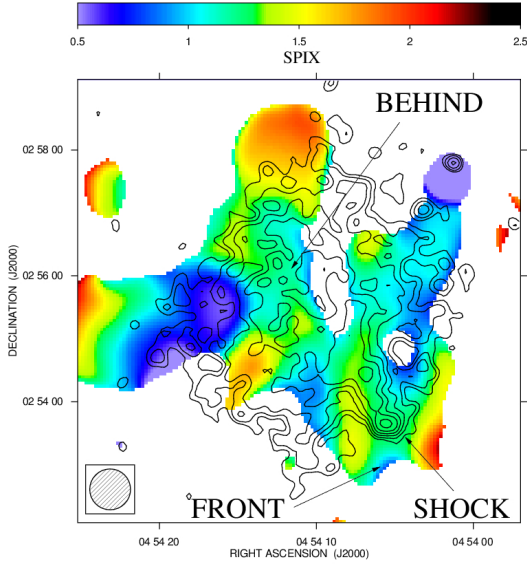
According to Murgia et al. (2009), the azimuthally averaged brightness profile of radio halos can be modeled with an exponential law:

$$I(r) = I_0 e^{-\frac{r}{r_c}} \quad (1)$$

Table 4. Fluxes of radio galaxies

Label	$S_{325\text{ MHz}}$ mJy	$S_{1400\text{ MHz}}$ mJy	$\alpha_{325\text{ MHz}}^{1400\text{ MHz}}$
A	$\lesssim 3.3$	6.4 ± 0.2	$\lesssim -0.5$
B	19 ± 1	5.2 ± 0.2	0.89 ± 0.06
C	84 ± 3	8.2 ± 0.3	1.59 ± 0.03
D	88 ± 3	23.2 ± 0.7	0.91 ± 0.03
E	90 ± 3	21.7 ± 0.7	0.97 ± 0.03
F	$\lesssim 3.0$	1.3 ± 0.1	$\lesssim 0.6$

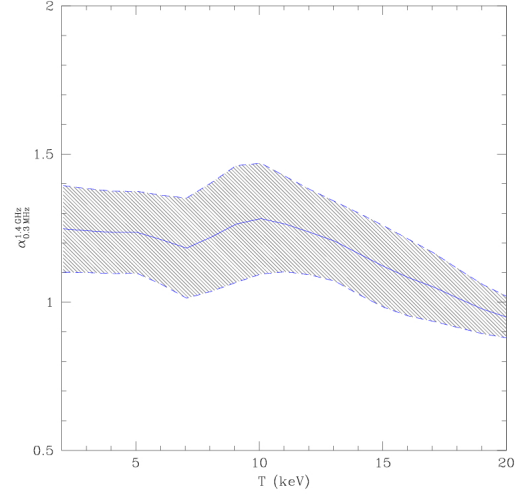
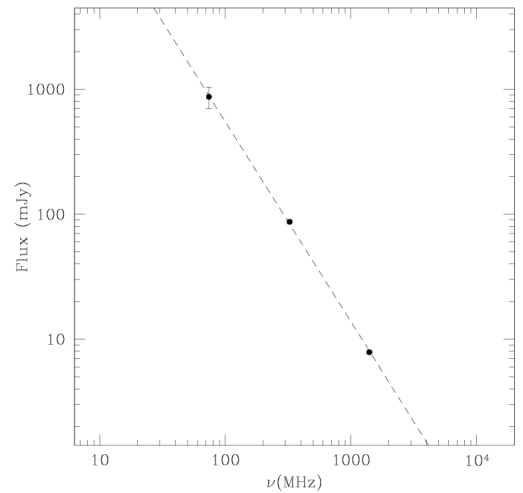
Col. 1: Radio galaxy label; Col. 2: Flux at 325 MHz; Col. 3: Flux at 1400 MHz; Col. 4: Spectral index between 325 and 1400 MHz.

**Fig. 8.** X-ray contours from the 0.8–4 keV X-ray image overlaid on the spectral index image of the radio halo at 39". The contours are spaced by a factor of $\sqrt{2}$.

where I_0 and r_e are the central radio surface brightness and the e -folding radius. From the central brightness and the e -folding radius, the radio emissivity of the diffuse emission can be inferred. This model does not account for the local deviations from the circular symmetry of the diffuse emission but gives a good description of averaged properties, involving a minimum set of free parameters and allowing a comparison with other radio halos. Murgia et al. note that it is a simplistic description and consider also more realistic pictures, as for example the injection model. According to this injection model, the radio halo brightness profile would be:

$$I(r_{\perp}) = I_0 \left(1 + \frac{r_{\perp}^2}{r_e^2} \right)^{-6\beta\eta+0.5} \quad (2)$$

where $I(r_{\perp})$ is the brightness value at the r_{\perp} projected distance from the cluster center and I_0 is the central radio halo brightness. The diffuse emission is supposed to be generated by an isotropic population of relativistic electrons with a power law energy spectrum and in a steady state of continuous injection. A radio halo spectral index $\alpha = 1$ is considered, corresponding to a perfect equipartition condition between particles and field (see Brunetti et al. 1997, Beck & Krause 2005). The magnetic field has been assumed to be completely tangled and an average over all the possible directions between the magnetic field and the

**Fig. 9.** Exponential smooth of the spectral index α between 325 and 1400 MHz versus thermal gas temperature T . We adopted a smoothing scale of 1 keV.**Fig. 10.** Spectral index of the source C (see e.g. Fig. 1, top right panel) between 74 and 1400 MHz.

line-of-sight has been performed. The magnetic field strength is assumed radially decreasing as a function of the thermal gas density, taken to follow a β -model (Cavaliere & Fusco-Femiano 1976).

By using the procedure implemented in the software FARADAY (Murgia et al. 2004), we tried to fit the azimuthally averaged radial profile of the radio halo in A520 both considering an exponential and an injection model. For the injection model, we adopted the gas density parameters derived by Govoni et al. (2001) from ROSAT X-ray data and re-scaled to our chosen cosmology ($n_e(0) = 3.8 \times 10^{-3} \text{ cm}^{-3}$, $r_c = 127'' = 413 \text{ kpc}$ and $\beta = 0.87$). In both cases the fits do not allow a good description of the data points. Indeed, the radial profile keeps flat up to distances from the cluster center $\sim 400 \text{ kpc}$, see Fig. 5. This peculiarity has been already noticed by Govoni et al. (2001) who do not exclude that this emission could actually be a peripheral source seen in projection towards the cluster center.

6. Discussion

6.1. Radio halo spectral index image

The spectral index image of the radio halo in A520 (Fig. 4) appears clumpy, with fluctuations both in the $39''$ and in the $60''$ resolution images. The distribution of the spectral index has a dispersion slightly larger than the mean value of the spectral index error image. This suggests that the measurement process significantly contributes to the observed fluctuations even if a certain degree of intrinsic clumpiness seems to be present. According to primary models of radio halo formation (e.g. Schlickeiser et al. 1987; Petrosian 2001; Brunetti & Lazarian 2007, 2011), magneto-hydro-dynamical turbulence due to cluster mergers is supposed to stochastically (re-)accelerate pre-existing electrons through Fermi-II processes causing diffuse large scale synchrotron radio emission in massive galaxy clusters. In this scenario, a complex cluster distribution of the spectral index is expected. On the contrary, secondary models of radio halo formation (e.g. Dennison 1980, Pfrommer et al. 2008, Ensslin et al. 2011) propose that the diffuse large scale synchrotron radio emission is due to a continuous generation of relativistic electrons through the collision between relativistic protons (accelerated during the cluster history) and thermal protons in the ICM. In this scenario, a uniform distribution of the radio halo spectral index is expected.

The intrinsic complexity observed in the radio halo spectral index image of A520 appears in agreement with the predictions from primary models, although secondary models can not be excluded. According to primary models a radial steepening and a complex spatial distribution of the spectral index is expected because of a different (re-)acceleration efficiency in different cluster regions and/or variations in the local magnetic field strength. Consequently, the presence of radial steepening in radio halo spectral index distribution would suggest that the outer regions of the radio halo are characterized by inefficient acceleration processes and/or the presence of a radial gradient in the magnetic field strength. Therefore, if interpreted in the context of a primary model scenario, the flatness in the spectral index of the radio halo in A520 could indicate a fine-tuning between the magnetic field strength and the power supply up to large ($\sim 1 \text{ Mpc}$) distances from the cluster center, in the radio halo periphery.

6.2. Shock wave

Feretti et al. (2004) found that the spectral index in A665 steepens at increasing distances from the cluster center, along the direction of propagation of the shock. The authors interpret this behavior as due to the fact that shocks associated with major merg-

ers are not strong enough to accelerate particles, as predicted by Gabici & Blasi (2003). The shocks in A665 and in A520 are characterized by the same Mach number ($M \sim 2$), therefore we would expect in A520 a similar behavior as observed in A665. On the contrary, in the hypothesis that major merger shocks are efficient in accelerating radiating electrons and since no turbulence or other kind of acceleration mechanisms are supposed to be present in between the shock and the North-East clump, Markevitch et al. (2005) expect different spectral index for these two regions and a steepening of the spectral index along the shock in A520, starting from a value of $\alpha = 1.2$ at the bow shock location.

By considering a sector along the direction of propagation of the shock and the cool tail in the NE, we measured a spectral index of ~ 1.2 that keeps flat. Even if we measure a spectral index $\alpha = 1.2$ at the bow shock location in agreement with the predictions from Markevitch et al. (2005), our analysis does not reveal the steepening of the spectral index in the direction of the propagation of the shock that they expect. The 1σ errors on spectral index rule out spectral steepening from SW to NE at a confidence level of $\sim 80\%$. Moreover, the significant spectral difference between the radio emission at the shock location and that in the NE that Markevitch et al. (2005) suppose seems not to be present.

The behavior of the spectral index distribution in A520 differs from that observed in A665 and indicates that some efficient powering mechanism is at work even at large ($\sim 1 \text{ Mpc}$) distances from the cluster center. The spectral slope observed at the shock location in A520 does not exclude shock-accelerated electrons, while the flatness of the spectrum along the direction of propagation of the shock and the absence of significant spectral differences between the SW and the NE of the diffuse emission could indicate the presence of turbulence in the intermediate region. An alternative possibility is that turbulence is powering the emitting particles up to distances of 1 Mpc from the cluster center.

Deep radio observations at higher resolution both at 1400 and at 325 MHz would allow to measure the spectral index distribution directly behind the location of the shock with an high degree of accuracy, giving precious information to distinguish between the two scenarios. Moreover, sensitive X-ray observations would allow to probe the possible presence of turbulence in the intermediate region and at $\sim \text{Mpc}$ distance from the cluster center (see e.g. Schuecker et al. 2004 for the Coma cluster).

6.3. Radio halo spectral index versus thermal gas temperature

To infer some information about a possible correlation between the radio and X-ray emission in the cluster, we compared the spectral index distribution with the thermal gas temperature image.

A520 follows the trend of the integrated spectral index versus temperature observed for other clusters. A strong point-to-point correlation between the radio-halo spectral index and the thermal-gas temperature is not present in A520, see Fig. 9. A similar case has been observed in MACSJ00717+3745 (Bonafede et al. 2009a). In that case the authors conclude that it is due to projection effects. A correlation between the distribution of the radio halo spectral index and the thermal gas temperature has been observed in the galaxy cluster A2744 (Orrù et al. 2007). In the case of A520, the absence of such a correlation could be due to the peculiarity of the diffuse emission and to the fact that it could actually be a source at the cluster periphery seen

in projection, as Govoni et al. (2001) noted, see the discussion in § 6.4.

6.4. Radio halo nature

The diffuse synchrotron emission in A520 has been originally classified as a cluster radio halo because of its location (Giovannini et al. 1999). The high resolution images of the radio halo at 1400 MHz (Fig. 1, top right and bottom panels) show that the brighter structures of the diffuse emission are located in the North-East of the cluster, at the same spatial location of the cool tail, and in the South-West of the cluster, aligned with the shock. In between, a depression in the radio surface brightness can be observed. A clear link is present between the mass distribution (Clowe et al. 2012) and the diffuse radio emission. Indeed, we note that the non-thermal emission permeates regions of high mass. The NE clump is aligned with the elongated mass distribution (NE to SW): structures 2+3 in Fig. 2 by Clowe et al. (2012). The diffuse emission at the shock location in the SW is observed in correspondence of the 4-7 structures in the same figure.

In contrast with most of the radio halos observed to date the azimuthally averaged brightness profile can not be modeled either with an exponential law or with a more realistic model based on the continuous injection of relativistic electrons (Murgia et al. 2009). Indeed, the brightness remains flat up to distances ~ 400 kpc from the cluster center. This flatness has been already noted by Govoni et al. (2001) who do not exclude that this is a source at the cluster periphery, apparently located at the cluster center because of projection effects. Another possible explanation could be that we are looking at a relic in the SW and a young still forming radio halo in the NE. In the past the cluster could have been crossed by several shocks, one of them is now powering the diffuse non thermal emission in the SW. Along the tail of the shock, turbulence due to the merger is allowing the formation of a radio halo. This would explain the absence of central peak in the radio emission. A similar emission has been observed in the cluster 1RXS J0603.3+4214 (van Weeren et al. 2012).

Typically, elongated relics are characterized by a filamentary structure that has not been observed in this case with the available data. Sensitive high resolution observations are necessary to rule out the presence of filamentary substructures. The spectral index of the emission in the SW edge does not show any obvious distribution. Elongated relics show a clear spectral steepening toward the cluster center, while a specific trend has not been detected in roundish relics (see Feretti et al. 2012). At present we do not have information about polarization properties of the source. The degree of polarization of the emission could be very useful in testing the relic scenario. A work where polarimetric properties will be analysed and discussed is currently in progress (Vacca et al. in preparation).

7. Conclusions

In this paper we presented the spectral index image of the radio halo at the center of the cluster A520, obtained by comparing VLA observations at 1400 and 325 MHz. We found an integrated spectral slope $\alpha_{325}^{1400} = 1.12 \pm 0.05$.

The clumpy morphology in the radio halo spectral index image supports the primary models of radio halo formation. In this framework, the flatness of the spectrum could suggest an ongoing merger phenomenon that uniformly and continuously (re-) accelerates relativistic electrons *in situ* up to the distance where the shock wave has been detected.

The integrated spectral index and the global thermal gas temperature are in good agreement with the trend observed in other galaxy clusters, although we do not observe a clear point-to-point correlation between the spectral index and the thermal gas temperature. The lack of this correlation can be explained in the context of the peculiar nature of the radio emission at the center of the cluster. This emission has been originally classified as a radio halo but the brightness profile of this source strongly differs from those observed in other radio halos. New deep polarimetric observations over a wide frequency range are necessary to better understand the nature of the diffuse emission in A520 and to investigate the connection between the thermal and non-thermal properties of this galaxy cluster.

Acknowledgements. We thank the referee for helpful comments and suggestions that improved the paper. The research was partially supported by PRININAF2009. The National Radio Astronomy Observatory (NRAO) is a facility of the National Science Foundation, operated under cooperative agreement by Associated Universities, Inc. Basic research in radio astronomy at the Naval Research Laboratory is supported by 6.1 Base funding.

References

- Akamatsu, H., Inoue, S., Sato, T., et al. 2013, PASJ, 65, 89
 Bacchi, M., Feretti, L., Giovannini, G., & Govoni, F. 2003, A&A, 400, 465
 Beck, R., & Krause, M. 2005, Astronomische Nachrichten, 326, 414
 Bonafede, A., Feretti, L., Giovannini, G., et al. 2009a, A&A, 503, 707
 Bonafede, A., Giovannini, G., Feretti, L., Govoni, F., & Murgia, M. 2009b, A&A, 494, 429
 Brentjens, M. A. 2008, A&A, 489, 69
 Brunetti, G., Setti, G., & Comastri, A. 1997, A&A, 325, 898
 Brunetti, G., & Lazarian, A. 2007, MNRAS, 378, 245
 Brunetti, G., Cassano, R., Dolag, K., & Setti, G. 2009, A&A, 507, 661
 Brunetti, G., & Lazarian, A. 2011, MNRAS, 410, 127
 Brunetti, G., Rudnick, L., Cassano, R., et al. 2013, A&A, 558, A52
 Brunetti, G., Rudnick, L., Cassano, R., et al. 2013, arXiv:1309.1820
 Carlberg, R. G., Yee, H. K. C., Ellingson, E., et al. 1996, ApJ, 462, 32
 Cassano, R. 2009, The Low-Frequency Radio Universe, 407, 223
 Cavaliere, A., & Fusco-Femiano, R. 1976, A&A, 49, 137
 Clowe, D., Bradač, M., Gonzalez, A. H., et al. 2006, ApJ, 648, L109
 Clowe, D., Markevitch, M., Bradač, M., et al. 2012, ApJ, 758, 128
 Condon, J. J., Cotton, W. D., Greisen, E. W., et al. 1998, AJ, 115, 1693
 Cooray, A. R., Grego, L., Holzapfel, W. L., Joy, M., & Carlstrom, J. E. 1998, AJ, 115, 1388
 Dennison, B. 1980, ApJ, 239, L93
 Ensslin, T. A. 2002, A&A, 396, L17
 Ensslin, T., Pfrommer, C., Miniati, F., & Subramanian, K. 2011, A&A, 527, A99
 Feretti, L., Giovannini, G., & Bohringer, H. 1997, New A, 2, 501
 Feretti, L., Orrù, E., Brunetti, G., et al. 2004, A&A, 423, 111
 Feretti, L., Giovannini, G., Govoni, F., & Murgia, M. 2012, A&A Rev., 20, 54
 Gabici, S., & Blasi, P. 2003, ApJ, 583, 695
 Giacintucci, S., Venturi, T., Brunetti, G., et al. 2005, A&A, 440, 867
 Giovannini, G., Feretti, L., Venturi, T., Kim, K.-T., & Kronberg, P. P. 1993, ApJ, 406, 399
 Giovannini, G., Tordi, M., & Feretti, L. 1999, New A, 4, 141
 Giovannini, G., Bonafede, A., Feretti, L., et al. 2009, A&A, 507, 1257
 Giovannini, G., Feretti, L., Girardi, M., et al. 2011, A&A, 530, L5
 Girardi, M., Barrera, R., Boschini, W., & Ellingson, E. 2008, A&A, 491, 379
 Govoni, F., Feretti, L., Giovannini, G., et al. 2001, A&A, 376, 803
 Govoni, F., Markevitch, M., Vikhlinin, A., et al. 2004, ApJ, 605, 695
 Greisen, E. W., Spekkens, K., & van Moorsel, G. A. 2009, AJ, 137, 4718
 Jee, M. J., Mahdavi, A., Hoekstra, H., et al. 2012, ApJ, 747, 96
 Kale, R., & Dwarakanath, K. S. 2010, ApJ, 718, 939
 Lane, W. M., Cotton, W. D., Helmboldt, J. F., & Kassim, N. E. 2012, Radio Science, 47, 0
 Mahdavi, A., Hoekstra, H., Babul, A., Balam, D. D., & Capak, P. L. 2007, ApJ, 668, 806
 Markevitch, M., Gonzalez, A. H., David, L., et al. 2002, ApJ, 567, L27
 Markevitch, M., Govoni, F., Brunetti, G., & Jerius, D. 2005, ApJ, 627, 733
 Murgia, M., Govoni, F., Feretti, L., et al. 2004, A&A, 424, 429
 Murgia, M., Govoni, F., Markevitch, M., et al. 2009, A&A, 499, 679
 Murgia, M., Parma, P., Mack, K.-H., et al. 2011, A&A, 526, A148
 Neumann, D. M., Arnaud, M., Gastaud, R., et al. 2001, A&A, 365, L74

- Ogrean, G. A., & Brüggen, M. 2013, MNRAS, 433, 1701
- Orrú, E., Murgia, M., Feretti, L., et al. 2007, A&A, 467, 943
- Parma, P., Murgia, M., de Ruiter, H. R., et al. 2007, A&A, 470, 875
- Perley, R. A. 1999, Synthesis Imaging in Radio Astronomy II, 180, 383
- Petrosian, V. 2001, ApJ, 557, 560
- Pfrommer, C., & Enßlin, T. A. 2004, MNRAS, 352, 76
- Pfrommer, C., Ensslin, T. A., & Springel, V. 2008, MNRAS, 385, 1211
- Pizzo, R. F., & de Bruyn, A. G. 2009, A&A, 507, 639
- Proust, D., Cuevas, H., Capelato, H. V., et al. 2000, A&A, 355, 443
- Russell, H. R., Sanders, J. S., Fabian, A. C., et al. 2010, MNRAS, 406, 1721
- Sarazin, C. L. 2002, Merging Processes in Galaxy Clusters, 272, 1
- Sarazin, C. L., Finoguenov, A., & Wik, D. R. 2013, Astronomische Nachrichten, 334, 346
- Scaife, A. M. M., & Heald, G. H. 2012, MNRAS, 423, L30
- Schlickeiser, R., Sievers, A., & Thiemann, H. 1987, A&A, 182, 21
- Schuecker, P., Finoguenov, A., Miniati, F., Böhringer, H., & Briel, U. G. 2004, A&A, 426, 387
- Struble, M. F., & Rood, H. J. 1999, ApJS, 125, 35
- Thierbach, M., Klein, U., & Wielebinski, R. 2003, A&A, 397, 53
- Vacca, V., Murgia, M., Govoni, F., et al. 2010, A&A, 514, A71
- van Weeren, R. J., Intema, H. T., Oonk, J. B. R., Röttgering, H. J. A., & Clarke, T. E. 2009, A&A, 508, 1269
- van Weeren, R. J., Roettgering, H. J. A., Brueggen, M., & Hoeft, M. 2010, Science, 330, 347
- van Weeren, R. J., Brüggen, M., Röttgering, H. J. A., et al. 2011, A&A, 533, A35
- van Weeren, R. J., Röttgering, H. J. A., Intema, H. T., et al. 2012, A&A, 546, A124
- Venturi, T., Giacintucci, S., Dallacasa, D., et al. 2013, A&A, 551, A24
- Vikhlinin, A., Markevitch, M., & Murray, S. S. 2001, ApJ, 551, 160
- Yee, H. K. C., Ellingson, E., & Carlberg, R. G. 1996, ApJS, 102, 269